Validation of GOES-16 ABI VNIR channel radiometric performance with NPP and NOAA-20 VIIRS over the Sonoran Desert

Xin Jing,[a,*] **Tung-Chang Liu**,[a] **Xi Shao**,[a,b] **Sirish Uprety**,[a]
Bin Zhang,[a] **and A. Surjalal Sharma**[b]
[a]University of Maryland, Cooperative Institute for Satellite Earth System Studies, Earth System Science Interdisciplinary Research Center, College Park, Maryland, United States
[b]University of Maryland, Department of Astronomy, College Park, Maryland, United States

Abstract. The advanced baseline imager (ABI) onboard Geostationary Operational Environmental Satellites-16 (GOES-16) provides high-quality visible and near-infrared (VNIR) imagery data. Radiometric performance of the GOES-16 ABI multiple VNIR bands (B1, B2, B3, B5, and B6) is evaluated over the Sonoran Desert by comparing measurements with Suomi National Polar-Orbiting Partnership (S-NPP) and NOAA-20 visible infrared imaging radiometer suite equivalent bands M3, M5, M7, M10, and M11, respectively. In order to minimize the uncertainties due to the difference in spectral response functions of similar bands from the different sensors, spectral band adjustment factor (SBAF) derived from Hyperion data over Sonoran Desert is used. The large viewing angle at the Sonoran Desert by ABI (56.34 deg) and a lack of comprehensive BRDF model at such viewing geometry are the main challenges for the comparison. Two schemes to address such challenges were developed. A data-derived (DD) method, based on confining the matched solar-zenith angle and view-zenith angle between ABI and VIIRS, interpolation in solar-zenithal and relative-azimuthal angles is developed to address this issue. It is shown that there is some residual bias for ABI B1 and its equivalent VIIRS M3 band, which is mainly due to unaccounted angular dependence of atmospheric scattering in this DD method. To address this issue, a radiative transfer modeling (RTM)-based method to account for atmospheric effects is developed to facilitate the comparison. The time series trending and mean bias of reflectance ratio between ABI and VIIRS measurements over the Sonoran Desert after SBAF and bidirectional reflectance distribution function corrections are derived to evaluate the radiometric performance of ABI with respect to net primary productivity and NOAA-20 VIIRS. The analysis shows that the radiometric biases of the five VNIR channels of GOES-16 ABI are all within 5% in comparison to the matched channels of NPP VIIRS after applying the RTM correction. The analysis also detects ~6% drop in the radiometric bias of GOES-16 ABI 0.64 μm channel after April 23, 2019, which can be traced to the implementation of a correction of the ABI B2 calibration coefficient around this date. Further, we evaluate the relative radiometric bias for the five VNIR channels between NPP and NOAA-20 VIIIRS using double difference method, and the comparison shows that NPP VIIRS has 2% to 3% higher bias than NOAA-20 VIIRS for these spectral bands. *© 2020 Society of Photo-Optical Instrumentation Engineers (SPIE)* [DOI: 10.1117/1.JRS.14.044517]

Keywords: geostationary operational environmental satellites-16; advanced baseline imager; radiometric calibration; radiometric bias; national polar-orbiting partnership; NOAA-20; visible infrared imaging radiometer suite.

Paper 200389 received May 20, 2020; accepted for publication Nov. 19, 2020; published online Dec. 4, 2020.

1 Introduction

Being the first satellite in the next generation of geostationary Earth-observing systems, Geostationary Operational Environmental Satellites-16 (GOES-16, formerly GOES-R before

---

*Address all correspondence to Xin Jing, xinjing@umd.edu reaching the geostationary orbit) of National Oceanic and Atmospheric Administration (NOAA) was successfully launched on November 19, 2016.[1–5] GOES-16 provides high spatial and temporal resolution imagery of the Earth through 16 spectral bands at visible and infrared (VNIR) wavelengths using its advanced baseline imager (ABI). The ABI provides imagery products with up to four times finer spatial resolution and five times finer temporal resolution compared to the previous GOES imager. The radiometric accuracy for ABI VNIR (B01 to B06) is required to be within 5%,[6,7] which is achieved through onboard radiometric calibration using solar diffuser. With its significantly improved spectral, spatial, and temporal resolution and radiometric quality, the ABI continues to provide valuable data for weather and climate and weather studies and greatly improve the capabilities for weather forecasting and environmental monitoring.

Imaging sensors can exhibit a significant change in their radiometric performance after launch as a result of many factors, including stresses associated with the launch, operating environment of the spacecraft, and aging of the sensors and their subsystems.[8] Due to ABI's significantly improved specification and quality, it is challenging, yet important, to monitor and maintain the calibration stability of the sensor.

In the past, several methods have been developed to detect and characterize radiometric bias and stability of geostationary imaging sensor and intercompare with sensors on low-Earth-orbiting satellites using pseudo-invariant calibration sites (PICSs). In Ref. 9, an intercalibration method over the Sonoran Desert for GOES-10/12 Imager 650 nm channel using Moderate Resolution Imaging Spectroradiometer (MODIS) equivalent spectral channel at GOES viewing/illumination geometries was developed to characterize the radiometric bias and its stability. In the same study, the MODIS reflectance was normalized using a polynomial function of solar zenith angle (SZA) and relative azimuth angle (RAA) to GOES viewing/illumination geometries, and the spectral band adjustment factor (SBAF) derived from Hyperion data were used to eliminate the spectral responses function (SRF) difference impact on the intercomparison. This calibration method yields an accuracy of ∼4% for GOES-10/12 650-nm channel using AQUA MODIS C6 data as a reference standard. However, since the work in Ref. 9 focused only on the 650-nm channel of GOES-10/12, which is affected by atmosphere scattering, there is a concern that if this method also can be used for GOES-16 ABI, which contains six VNIR channels, and if this method can fix the atmospheric scattering properly.

There have been several studies to evaluate the radiometric bias of VNIR channels of GOES-16 ABI.[10–12] In Ref. 10, preliminary validation and intercomparison results for GOES-16 ABI bands (B1 to B3, B5, and B6), using the Radiometric Calibration Test Site (RadCaTS) were summarized. The ratio of the TOA spectral radiance for each ABI band to the ground-based RadCaTS results indicated that in general, the sensor spectral radiance was higher than those determined with RadCaTS, except for ABI band 6 (2243 nm). However, the BRDF correction for GOES-16 has not been investigated and no temporal trending is provided in the results. In Ref. 11, validation of the radiometric accuracy of five VNIR channels of GOES-16 ABI was performed using Uyuni Desert-based vicarious calibration through comparison with National Polar-Orbiting Partnership (NPP) visible infrared imaging radiometer suite (VIIRS) measurements. Regardless of the precipitation events in late February and early March in 2017 and several jumps in solar calibration coefficients, the reflectance from the ABI and VIIRS over two Uyuni targets were stable. However, the reflectances at the ABI bands 1 and 2 were shown to be 5% brighter than the VIIRS data, probably because no viewing/solar geometry correction or SBAF was applied. In Ref. 12, GEO-LEO intercomparison was performed using Simultaneous Nadir Overpasses (SNO) between GOES-16 ABI and VIIRS instruments and quantified the radiometric consistency between VIIRS instruments onboard NPP and NOAA-20, and double differencing was used to quantify the radiometric consistency between the two VIIRS instruments using ABI as the transferring radiometer. In Ref. 12, region of interest (ROI) for each SNO event was defined as a rectangular region ranging ±20 deg latitude and ±20 deg longitudes from the center of the GOES-16 subsatellite location (0 deg, −75 deg). Angular and spatial uniformity, ocean restrictions, and SBAF correction derived from scanning imaging absorption spectrometer for atmospheric chartography (SCIAMACHY) were applied in Ref. 12 to reduce uncertainty in the GEO-LEO intercomparison. The results suggested that ABI is consistent with NPP/VIIRS to be within 5% for band 1 and within 2% for the rest of the bands as of August 2019, except the cirrus band, i.e., B4. This work also found that the radiometric biases between NOAA-20 and NPP VIIRS bands are mostly 2% and 3% for the ABI-equivalent VNIR bands. Analysis in Ref. 12 was limited to the measurements made at solar noon to minimize the uncertainties due to shadowing effects on the surface. GEO-LEO SNO method is limited to the ABI nadir cases. No trending analysis of the radiometric bias was provided in Ref. 12.

The purpose of this study is to independently and alternatively assess the radiometric performance of GOES-16 ABI VNIR channels with respect to the NPP and NOAA-20 VIIRS using measurements over the Sonoran Desert. In order to minimize the uncertainties due to the difference in spectral response functions of different sensors, SBAF derived from Hyperion data over the Sonoran Desert is used. Unlike[12] which uses SCIAMACHY, this study is limited to a smaller region and hence the large footprint of SCIAMACHY (~200 km) can lead to higher uncertainties in spectral difference correction. Thus, Hyperion data that have high spatial resolution of nearly 30 m are used. To minimize the uncertainty due to viewing/solar geometries, i.e., BRDF characterization of the Sonoran Desert, a data-derived (DD) method based on the method introduced in Ref. 9 and a radiative transfer modeling (RTM)-based correction method are applied. Both time series and mean reflectance ratio between ABI and VIIRS measurements after SBAF and geometry-related corrections are used to evaluate the radiometric performance of ABI. In addition, radiometric consistency between the two VIIRS instruments is also evaluated through double-differencing using ABI as a reference.

This paper is organized as follows. In Sec. 2, the Sonoran Desert site and the sensor data analyzed in this paper are introduced. Section 3 describes the data processing steps and methodologies to conduct the study. In Sec. 4, the radiometric performance of GOES-16 ABI VNIR channels is evaluated through comparison with the measurements of VIIRS over the Sonoran Desert region. Conclusions are summarized in Sec. 5.

2 Site and Sensor Overview

2.1 *Sonoran Desert*

The Sonoran Desert is one of the largest North American deserts and has been recommended as one of the best PICSs in North America for VNIR bands.[13,14] It is a large flat region with limited vegetation cover and average altitude of ~0.2 km above sea level and has horizontal visibilities of 30 to 45 km. As a PICS, the Sonoran Desert is selected for intercomparison based on satellite measurements since it has a spatially uniform area large enough to accommodate the sampling of a large number of pixels and to minimize atmospheric adjacency effects due to light scattered from outside of the target region. Based on the previous research work on this site, the ROI selected for this study is located at 32.05° N–32.35° N, 114.4° W–W−114.7° W.[9,13–15] Figure 1(a) shows the map of the Sonoran Desert area from Google Earth and (b) the typical Sonoran Desert TOA reflectance spectra from Hyperion are used as representative of the 28×33 km rectangle area shown as the red rectangle in Fig. 1(a).

2.2 *GOES-16 ABI*

The ABI is the primary instrument aboard GOES-16 and represents the next generation VNIR and infrared (IR) imager at geosynchronous orbit. The GOES-16 was launched on November 19, 2016 and was in operation initially at around 89.5-deg west longitude where it was undergoing an extended testing and validation phase and then moved to 75.2-deg west longitude as GOES-east on December 18, 2017, to cover the Eastern American continental regions. The ABI onboard GOES-16 has 16 multispectral channels, including 6 VNIR, and 10 thermal emissive bands, and is capable of generating full-disk imagery every 5, 10, and 15 min. The spatial resolution varies from 0.5 to 2 km for different spectral channels. The six VNIR channels of GOES-16 ABI cover spectral range from 470 to 2250 nm with spatial resolution varying from 0.5 to 2.0 km. Since ABI B4 channel is a cirrus channel, only the window VNIR channels (B1 to B3, B5, and B6) are evaluated in this work. Table 1 summarizes the detailed specifications of ABI VNIR channels.

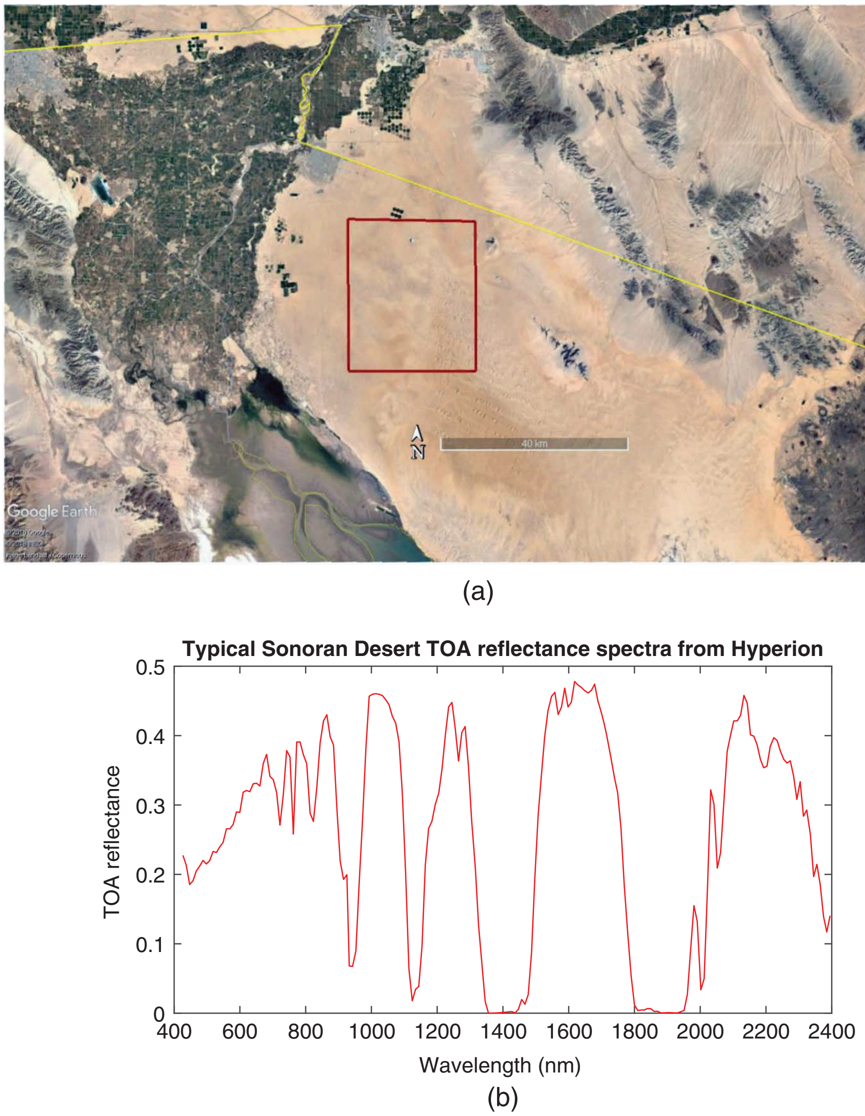

(a)

(b)

Fig. 1 (a) Map of the Sonoran Desert from Google Earth and (b) the typical Sonoran Desert TOA reflectance spectra from Hyperion on 2011-10-07.

Table 1 Center wavelengths and resolutions of the bands of GOES-16 ABI, NPP VIIRS, and NOAA-20 VIIRS sensors.

	GOES-16/ABI			NPP and NOAA-20/VIIRS			
Launch	November 19, 2016			October 28, 2011 and November 18, 2017			
	Central wavelength (nm)	Wavelength (nm)	Spatial resolution (km)		Central wavelength (nm)	Wavelength (nm)	Spatial resolution (km)
B1	470	450 to 490	1	M3	488	478 to 498	0.75
B2	640	590 to 690	0.5	M5	672	662 to 682	0.75
B3	865	846 to 885	1	M7	865	846 to 885	0.75
B5	1600	1580 to 1640	1	M10	1610	1580 to 1640	0.75
B6	2200	2225 to 2275	2	M11	2250	2250 to 2275	0.75

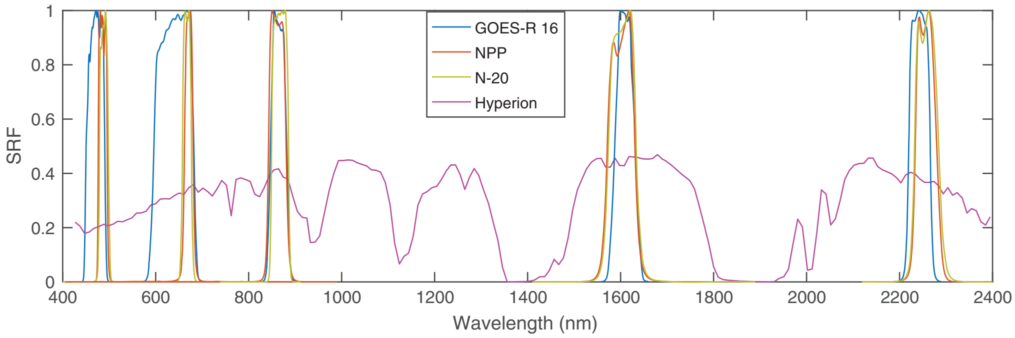

Fig. 2 Spectral response functions of GOES/ABI, NPP/VIIRS, and NOAA-20/VIIRS.

For the reflective solar bands, the conversion from radiance L to reflectance factor ρ_f is computed as[16]

$$\rho_f = \kappa L_v, \tag{1}$$

where κ is the "kappa factor." The kappa factor $\kappa = (\pi \cdot d^2)/E_{\text{sun}}$ represents the incident Lambertian-equivalent radiance, d is the instantaneous Earth–Sun distance (in astronomical units) and E_{sun} is the solar irradiance in the respective band [in $\mathrm{W}/(\mathrm{m}^2\mu\mathrm{m})$]. The kappa factor is included in the product metadata as the variable "kappa0." Then GOES-16 ABI reflectance ρ_{GOES} at a given location is computed as

$$\rho_{\text{GOES}} = \frac{\rho_f}{\cos(\theta_s)}, \tag{2}$$

where θ_s is the local SZA.

2.3 *NPP/NOAA-20 VIIRS*

The NPP satellite was launched on October 28, 2011. JPSS-1, now known as NOAA-20, is the second spacecraft in NOAA's next generation of polar-orbiting satellites and was launched on November 18, 2017. Both NPP and NOAA-20 carry the VIIRS, a 22-band visible/IR sensor, and cross the equator at about 01:30 and 13:30 local time, covering the entire Earth twice daily. The 11 VNIR moderate resolution channels of NPP and NOAA-20 VIIRS cover spectral range from 410 to 2257 nm with spatial resolution of 0.75 km. The moderate-resolution bands have 3200 pixels across scan within a scan angle of ±56.28 deg from nadir.[17–19] VIIRS sensor data record for M3, M5, M7, M10, and M11 bands with viewing zenith angles (VZAs) similar to GOES-16 ABI, in a range of the GOES nominal VZA of ±10 deg, from January 2018 to December 2019 between 19:30 and 21:30 UTC is used in this work to evaluate the radiometric performance of GOES-16 on the Sonoran Desert site. The VIIRS bands used in the study, central wavelength, and resolution information are summarized in Table 1. Figure 2 shows the spectral response functions of five equivalent bands of ABI and VIIRS.

2.4 *Hyperion*

Hyperion is a push-broom hyperspectral sensor aboard the Earth Observing-1 (EO-1) satellite, which images in 242 bands (196 of which are onboard calibrated[20]) covering the 400 to 2500 nm spectral range, at a nominal 10 nm spectral resolution and 30 m spatial resolution over a 7.7-km-wide swath. EO-1 began drifting to earlier equatorial crossing times[21,22] when its fuel supply was exhausted in late 2011. It was reported that Hyperion blue band region exhibits the statistically significant yearly drift and gain.[23] Therefore, this work applies the Hyperion yearly drift and gain/bias calibration correction coefficients provided by Ref. 23 before processing. The SRFs of the GOES 16 channels and VIIRS equivalent channels are plotted in Fig. 2. The Hyperion hyperspectral reflectance (yellow line) is overlapped with the spectral response function of the

GOES-16 B1, B2, B3, B5, and B6 channels (black line) and VIIRS equivalent channels (blue line for NPP and red line for NOAA-20). The SRFs of NPP and NOAA-20 VIIRS are almost identical. The SRFs of ABI B1 and B2 are much wider than those of VIIRS corresponding channels.

3 Data Processing

The data processing schemes employed in the GEO-LEO intercomparison analysis carried out in this paper consist of confine the observations in as close geometries as possible and preprocessing of LEO and GEO measurements to remove cloud and correction using DD or RTM method. Figure 3 shows the flowchart of the procedure used in this study. First, to limit the impact of varying observation time and view geometry on the radiometric bias evaluation, only observations around 1:30 p.m. local time and with view zenith angle difference of VIIRS-east versus ABI within ±10 deg are used for the LEO-GEO comparison. Then cloud/shadow contamination method from Ref. 9 has been applied to screen out the measurements contaminated by cloud or shadow. In addition, since view azimuth angle of VIIRS over Sonoran Desert is confined within a range, the relative difference between solar and view azimuth angle are confined to be between 105 deg and 140 deg for both VIIRS and ABI observations to be selected for the comparison. After preprocessing the LEO and GEO data, either DD or RTM correction method is combined with SBAF correction to evaluate the LEO-GEO radiometric bias. The DD or RTM correction method is used in this work to remove the impacts of residual viewing geometry difference between GOES-16 ABI and NPP/NOAA-20 VIIRS.

3.1 *Angular Limitation*

Figures 4(a)–4(c) show the radial plot of solar and viewing geometry over the Sonoran Desert for GOES-16/ABI, S-NPP/VIIRS, and NOAA-20/VIIRS, respectively. The VZA and viewing azimuth angle (VAA) with respect to ROI of GOES 16 ABI are fixed at 55.35 deg and 123.00 deg, respectively, observing target from east direction. The NPP and NOAA-20, on the other hand, have variable viewing angles and observed the target ROI from both east and west directions. Since there is a substantial overlap in solar geometry distribution among GOES-16/ABI, NPP/VIIRS, and NOAA-20/VIIRS, i.e., areas marked with blue star in Figs. 4(a)–4(c) are in the same region, the main challenge here is to account for the difference in VZA and apply

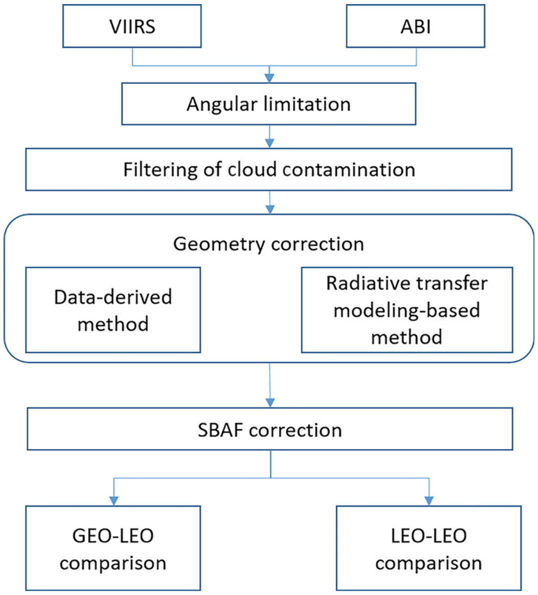

Fig. 3 Flowchart of the DD and RTM-based validation scheme for GOES-16 ABI VNIR channel radiometric calibration.

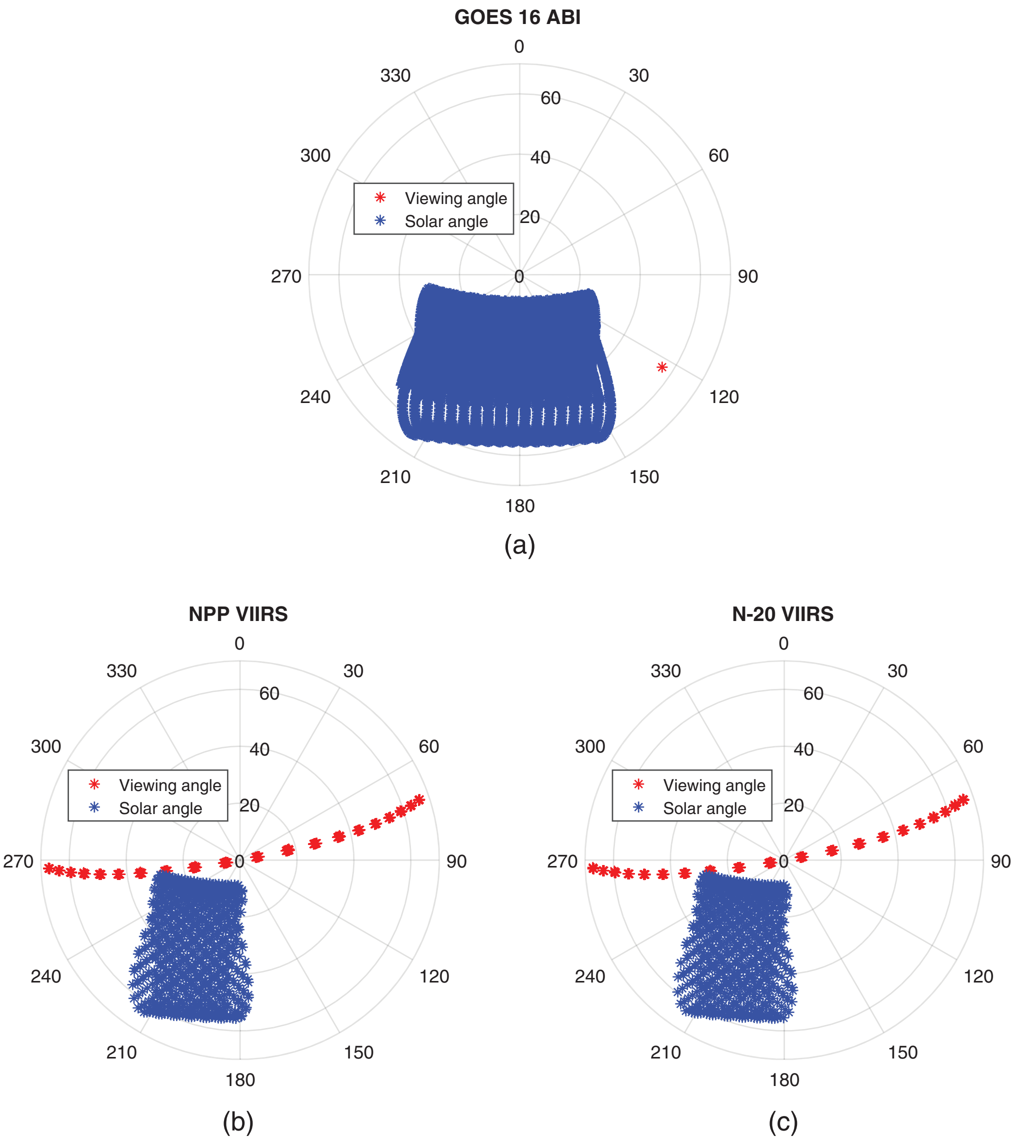

(a)

(b)

(c)

Fig. 4 Solar (blue) and viewing (red) angular distribution of (a) GOES-16, (b) NPP, and (c) NOAA-20. The angular direction (degrees east of north) in polar coordinate indicates azimuth angle and the length of the radius specifies the zenith angle.

the viewing-solar relative angle correction to the TOA reflectance. Note that cloud contamination filtering has been applied to the data shown in Sec. 3.1 in order to better illustrate the processing of geometric constraints.

As mentioned above, the ABI generates full-disk imagery every 5 (mode 4), 10 (mode 6), and 15 (mode 3) min. To reduce the impact due to solar azimuth angle and SZA variations, the local time selected for ABI observations is around 1:30 p.m. to match the overpassing time of SNPP and NOAA-20 VIIRS. Figure 5 plots the time series reflectance ratio derived from matched GOES-16 ABI and SNPP/NOAA-20 VIIRS observations after the applications of cloud contamination filtering and with the same local time restriction. The most notable pattern in Fig. 5 is the yearly cycle in the time series of reflectance ratio data of all five bands. The annual oscillation is of particularly large amplitude for B1 and B2 of ABI. Such an annual oscillation is most likely due to the viewing geometry difference between ABI and VIIRS and requires further analysis. Another notable feature in Fig. 5 is the scatter in the ABI B6 reflectance ratio during summer over the Sonoran Desert. This can be caused by weak incident solar radiation at the spectral region around wavelength 2200 nm.

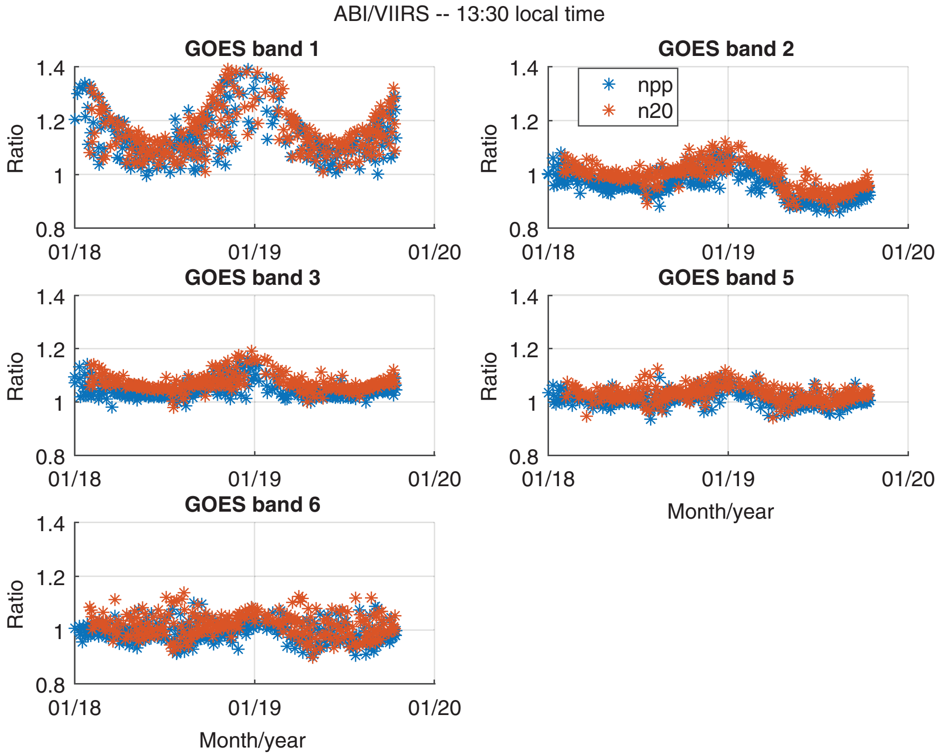

Fig. 5 Time series of reflectance ratio of GOES-16 ABI and SNPP/NOAA-20 VIIRS at 1:30 p.m. local time after cloud shadow contamination filtering.

Considering both the need for sufficient data points and the need to control for reflectance bias due to large VZA differences, only observations with VZA differences within ±10 deg between VIIRS-east versus ABI are used for comparison to reduce potential BRDF impact. In addition, since VAA of VIIRS over the Sonoran Desert is confined within a range, the RAA between solar azimuth angle and VAA for VIIRS changes between 105 deg and 140 deg in a year, and consequently only GOES ABI observations with RAA within 105 deg and 140 deg are used for the comparison. After the angular restrictions have been applied, there are 76 and 83 observation cases over 2018 and 2019 left for GOES/NPP and GOES/NOAA-20 matching pairs, respectively. Figures 6(a)–6(c) show the radial plot of solar and viewing geometry for GOES-16/ABI, NPP/VIIRS, and NOAA-20/VIIRS, respectively, after applying the angular restrictions on VZA and RAA. Next, both (DD method and RTM-based methods are introduced to further correct BRDF and atmospheric effects on the intersensor reflectance ratio independently.

3.2 *Filtering of Cloud/Shadow Contamination*

To screen out cloud and cloud shadow effects, the screening method proposed in Ref. 9 is modified and used in this study. The procedure of contamination screening includes two steps: first, the thresholds derived from the reflectance histogram are used to remove the outlier sensor pixels that are contaminated by cloud or shadow; second, a recursive filtering method is applied to further remove the abnormal observations with partial cloud/shadow contaminations.

Yu et al.[9] focused on visible channels under the assumption that cloud reflectance in the visible wavelength is generally higher than the reflectance of desert bare ground, which in turn is higher than wet soil and vegetation, so the inflection points of reflectance histogram curve at two sides of the histogram tails were used as the thresholds.[9,24] In this work, however, the impact of soil and vegetation on the TOA reflectance is different because the desert ROI and GOES-16 ABI VNIR channels used cover not only visible wavelength but also near-infrared (NIR) wavelength. For NIR channels, the cloud reflectance is generally lower than the desert bare ground. To avoid undesired removal of uncontaminated reflectance data, a modified reflectance histogram

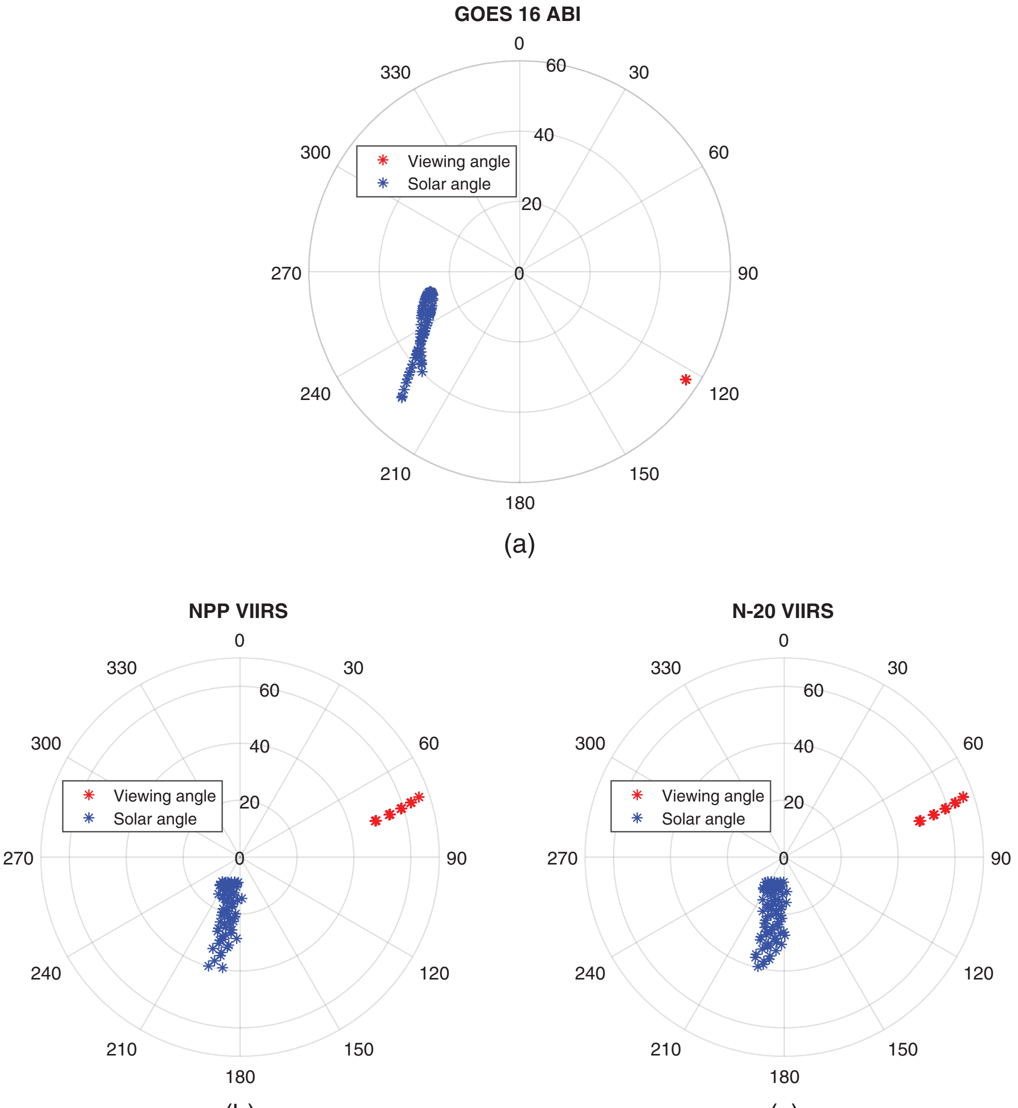

(a)

(b)

(c)

Fig. 6 Solar (blue) and viewing (red) angular distribution of (a) GOES-16, (b) NPP, and (c) NOAA-20 after applying the angular restrictions on VZA and RAA.

threshold method is applied. First, the integer portion of the square root of the reflectance number of each channel is taken as the first set of bins. Then the reflectivity data are binned and counts in each bin that are less than the square root of the data numbers of each channel are identified as anomalies and eliminated. Figure 7 shows an example of GOES-16 B1 reflectance histograms before and after the anomaly removal. After anomaly removal, the reflectance data with large nonreasonable value have been removed. Note that given the different bin numbers for reflectance before and after anomaly removal, the frequencies of bins for the same reflectance level before and after anomaly removal are different. About 18%, 24%, and 19% of the GOES-16, NPP and NOAA-20 observations, respectively, are identified as highly cloud/shadow contaminated and filtered out with this modified histogram threshold method.

Second, the reflectance data that pass the filtering using the threshold method are further processed with a recursive filtering. This filtering method is proposed in Ref. 9 and its general concept is based on the functional relationship between the reflectance factor and SZAs.[25] In Ref. 9, reflectance factor was defined as reflectance multiplied by the cosine of the SZAs. There is a strong functional relationship between advanced along-track scanning radiometer reflectance factor and the SZA over the desert sites[25] and is also applicable to the ABI and VIIRS data at the Sonoran Desert:

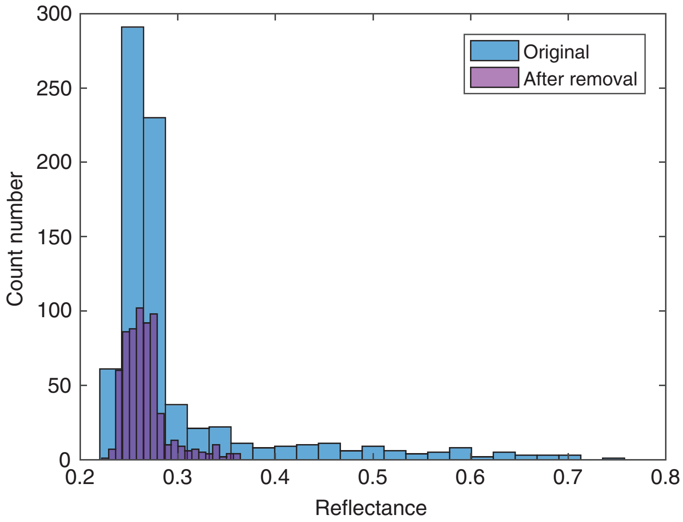

Fig. 7 Reflectance histograms of GOES-16 B1 with and without anomaly removal using the modified reflectance histogram method. Note the bin width has been refined during the anomaly removal process.

$$\rho_{\text{sensor}} \times \cos(\theta_s) = a + b \times \theta_s + c \times \theta_s^2, \tag{3}$$

where ρ_{sensor} is ABI or VIIRS reflectance, θ_s is the SZA of ABI or VIIRS data, and (a, b, and c) are fitting coefficients.

The data with maximum residual of the polynomial fitting regression to the left term of Eq. (3) and with SZAs above a predefined threshold are identified as contaminated observations and are removed from the dataset. Each removal of the outlier will result in a new fitting regression and a new set of residual removal until all residuals of the regression pass the threshold. More details of this recursive filtering method can be found in the papers.[9,26] Take NPP VIIRS M3 as an example, Fig. 8 shows the functional relationship between the left term of Eq. (3) and SZA for NPP VIIRS M3 data over ROI (a) before and (b) after the recursive filter is applied. After applying recursive filtering, outliers are removed and the residuals decrease from 8.436% (a) to 4.709% (b). About 17%, 13%, and 8% of the ABI, NPP, and NOAA-20 observations, respectively, are identified as outliers and filtered out with this recursive filtering method.

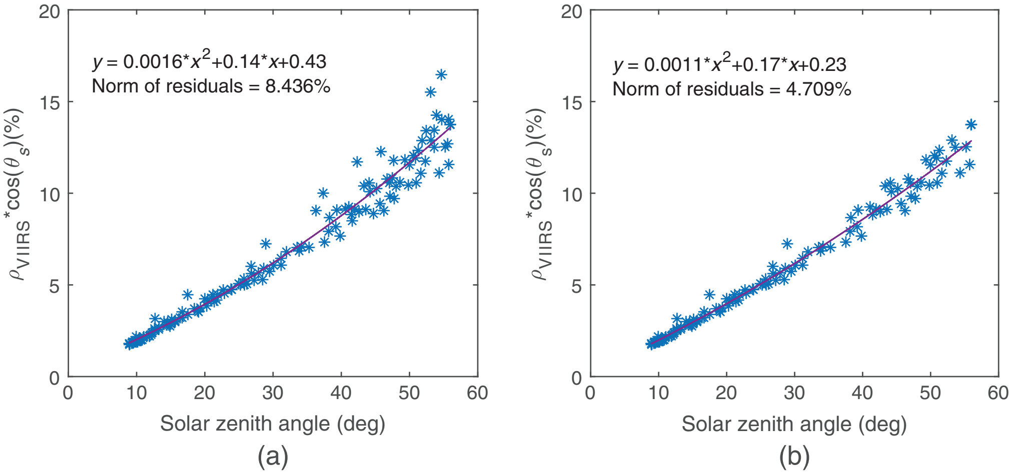

Fig. 8 Polynomial relationship between the reflectance factor and SZA for NPP/VIIRS M3 ROI data (a) before and (b) after the recursive filter is applied.

3.3 *Spectral Band Adjustment Factor Calculation*

The differences in SRF between sensors lead to a systematic radiometric offset when attempting cross calibration between them as two sensors respond differently to the same radiation source.[27,28] The cross calibration of VNIR sensors in this study requires the calculation of the SBAF to compensate for the intrinsic differences in sensor TOA response caused by SRF mismatches. The SBAF factor can be calculated by integrating the SRF of the sensor with the TOA reflectance profile from hyperspectral sensor observations. The Hyperion data are used, with the hyperspectral TOA reflectance:

$$\mathrm{SBAF}_{\lambda} = \frac{\overline{\rho_{\lambda,\mathrm{GOES}}}}{\overline{\rho_{\lambda,\mathrm{VIIRS}}}} = \frac{\dfrac{\int \rho_H(\lambda)\mathrm{RSR}_{\mathrm{GOES}}(\lambda)\mathrm{d}\lambda}{\int \mathrm{RSR}_{\mathrm{GOES}}(\lambda)\mathrm{d}\lambda}}{\dfrac{\int \rho_H(\lambda)\mathrm{RSR}_{\mathrm{VIIRS}}(\lambda)\mathrm{d}\lambda}{\int \mathrm{RSR}_{\mathrm{VIIRS}}(\lambda)\mathrm{d}\lambda}}, \tag{4}$$

where $\mathrm{RSR}_{\mathrm{GOES}}(\lambda)$ and $\mathrm{RSR}_{\mathrm{VIIRS}}(\lambda)$ are the RSR of GOES and VIIRS, respectively, for band with wavelength λ; $\rho_H(\lambda)$ is the Hyperion TOA spectral reflectance, which has been calibrated with gain and bias coefficients from Ref. 23 and corrected with yearly drift correction; and are the reflectance obtained from integrating the RSR of the GOES and VIIRS, respectively, with the spectral reflectance from Hyperion observation over the ROI.

Due to Hyperion limited regional coverage, only six cloud free Hyperion observations over the Sonoran ROI region have been collected covering years 2011 and 2012. Table 2 lists the SBAFs for GOES/S-NPP and GOES/NOAA-20 calculated with Eq. (4) from six Hyperion spectral profiles. The mean and standard deviation of six cases for GOES/S-NPP and GOES/NOAA-20 are also calculated. It can be seen that the largest standard deviation among all the channels is 0.0064 for GOES B6/NOAA-20 M11 pair so the Sonoran Desert SBAF can be taken as a constant and the mean SBAF is used in this work. Because the GOES/B1 and GOES/B2 have large RSR difference from their VIIRS counterpart channels (M3 and M5) as shown in Fig. 2, and they are at the large slope region in the Hyperion TOA reflectance spectra, they have the largest SBAF for the Sonoran Desert.

Convolution errors due to the low spectral resolution of the Hyperion were evaluated given that the spectral resolution of the Hyperion is 10 nm, whereas the band width of the ABI/VIIRS sensor is as narrow as 20 nm. First, MODTRAN is used to simulate TOA reflectance (built-in surface desert reflectivity) with different spectral resolutions, i.e., 10 nm (Hyperion spectral resolution) and 1 nm (fine spectral resolution). Then the reflectances of these two spectral resolutions are convolved with three sensors spectral response functions. The reflectance biases introduced by different spectral resolutions are 0.02%, −0.05%, −0.28%, 0.01%, and 0.03% of ABI B1, B2, B3, B5, and B6, respectively, according to Eq. (10) or Eq. (11).

Table 2 SBAFs for GOES/NPP and GOES/NOAA-20

	GOES/NPP					GOES/NOAA-20				
	B1/M3	B2/M5	B3/M7	B5/M10	B6/M11	B1/M3	B2/M5	B3/M7	B5/M10	B6/M11
20110729	0.9528	0.9252	1.0084	1.0061	1.0318	0.9485	0.9509	1.0009	1.0037	1.0359
20111007	0.9543	0.9289	1.0040	1.0053	1.0272	0.9498	0.9479	1.0033	1.0027	1.0289
20120518	0.9518	0.9309	1.0032	1.0034	1.0235	0.9473	0.9485	1.0038	1.0013	1.0251
20120608	0.9502	0.9309	1.0041	1.0052	1.0222	0.9454	0.9498	1.0032	1.0028	1.0236
20121216	0.9580	0.9235	1.0042	1.0054	1.0365	0.9544	0.9439	1.0037	1.0026	1.0390
20121224	0.9558	0.9212	1.0047	1.0057	1.0370	0.9517	0.9423	1.0033	1.0027	1.0394
Mean	0.9538	0.9268	1.0048	1.0052	1.0297	0.9495	0.9472	1.0030	1.0026	1.0320
STD	0.0026	0.0037	0.0017	0.0009	0.0058	0.0029	0.0031	0.0010	0.0007	0.0064

3.4 *Viewing Geometry Correction*

3.4.1 *Data-derived method*

Even though the local time selected for ABI observations is around 1:30 p.m. to match the overpassing time of SNPP and NOAA-20 VIIRS, the solar zenith difference between ABI and VIIRS changes within 10 deg to 17 deg. To eliminate the potential uncertainty caused by the effect of SZA on reflectance, we adopt the method based on fitting the reflectance as a function of SZA and RAA that was applied in Ref. 9 in this work. The observed reflectance for both ABI and VIIRS are normalized as

$$r_\lambda(\varphi) = \frac{R_\lambda(\varphi)}{\text{mean}[R_\lambda(\varphi)]}, \tag{5}$$

where $R_\lambda(\varphi)$ is the reflectance at RAA $= \varphi$ for band with wavelength λ, and $r_\lambda(\varphi)$ is the corresponding normalized reflectance.

Then the variation of normalized reflectance is fitted as a function of φ:

$$\begin{aligned} r_\lambda(\varphi) = a_0 &+ [a_{1,0} + a_{1,1}\,\cos(\theta_s) + a_{1,2}\,\cos(\theta_s)^2] \times \cos(\varphi) \\ &+ [a_{2,0} + a_{2,1}\,\cos(\theta_s) + a_{2,2}\,\cos(\theta_s)^2] \times \cos(2\varphi), \end{aligned} \tag{6}$$

where a_0, $a_{1,0}$, $a_{1,1}$, $a_{1,2}$, $a_{2,0}$, $a_{2,1}$, and $a_{2,2}$ are the fitting parameters derived with least square fitting, and θ_s is the SZA.

Since the BRDF correction-factor is directly derived from sensor observation and geometry information, this method is referred to as DD method. The DD correction factor each matching band with wavelength λ is given by

$$R_{c,\lambda,\text{VIIRS,ABI}} = \frac{r_{\lambda,\text{ABI}(\varphi_{\text{ABI}},\theta_{s,\text{ABI}})}}{r_{\lambda,\text{VIIRS}(\varphi_{\text{VIIRS}},\theta_{s,\text{VIIRS}})}}, \tag{7}$$

where $r_{\lambda,\text{ABI}(\varphi_{\text{ABI}},\theta_{s,\text{ABI}})}$ and $r_{\lambda,\text{VIIRS}(\varphi_{\text{VIIRS}},\theta_{s,\text{VIIRS}})}$ are the BRDF factor for GOES and VIIRS as function of RAA $= \varphi_{\text{ABI}}$, VZA $= \theta_{s,\text{ABI}}$, and RAA $= \varphi_{\text{VIIRS}}$ VZA $= \theta_{s,\text{VIIRS}}$ for band with wavelength λ, respectively.

ABI B1 is the shortest wavelength channel among the five bands of interest and largely affected by atmospheric scattering. In addition, this ABI channel has relatively large SBAF compared with VIIRS equivalent channel (Table 2) and there is unaccounted bias between ABI B1 and VIIRS M3 due to atmospheric transmission path difference in addition to the viewing geometry difference. As we will show in Sec. 4.1, a direct RAA and SZA-based fitting in DD-method results in unphysically large bias between ABI B1 and VIIRS M3. Therefore, we also introduce and evaluate another viewing geometry correction method based on RTM to address the deficiency in the DD method.

3.4.2 *Radiative transfer modeling-based method*

An alternative intercomparison method based on RTM is described in this section. Given ABI and VIIRS have similar solar geometry over the Sonoran Desert after constraining the observations to be around the same local time, the Sun-to-Earth atmospheric transmission paths for ABI and VIIRS are the same. To eliminate the difference due to the atmosphere on Earth sensor and the difference in view geometry, another correction method is derived in this work using RTM-based, i.e., MODTRAN, simulations. The radiative transmission modeling-based correction factor to account for Earth-to-sensor path difference can be represented by a proportionality relation between TOA radiance and direct-ground-reflected radiance:

$$f_{\lambda,\theta_v,\theta_s,\varphi} = \frac{L_{\lambda,\theta_v,\theta_s,\varphi}}{l_{\lambda,\theta_v,\theta_s,\varphi}}, \tag{8}$$

where $f_{\lambda,\theta_v,\theta_s,\varphi}$ is the Earth-to-sensor atmospheric transmission correction factor with given RAA (φ), SZA (θ_s), and VZA (θ_v) for a channel with central wavelength λ, $L_{\lambda,\theta_v,\theta_s,\varphi}$ and $l_{\lambda,\theta_v,\theta_s,\varphi}$ are the MODTRAN-derived channel TOA radiance and ground reflected radiation directly transmitted to the sensor (direct-ground-reflected radiance) in units of $\mathrm{W/cm^2\,sr}$ for the channel with central wavelength λ, respectively.

The ROI in our work is relatively flat with very limited vegetation cover,[9,29] so the impact of topography is ignored. Parameters such as RAA, VZA, SZA for each matched pair of ABI-VIIRS observations, and SRFs of GOES-16 ABI, NPP VIIRS, and NOAA-20VIIRS are inputs for MODTRAN simulation. Moreover, U.S. Standard Atmosphere (1976) profile and spectral albedo of desert surface are used in the RTM simulation. Since ABI B1 is very sensitive to aerosol loading in the atmosphere, we acquired aerosol optical depth (AOD) data at 550 nm over the Sonoran Desert from CAMS reanalysis dataset,[30] and it changes between 0.01 and 0.13 on the days that VIIRS and ABI intersected. Sensitivity calculation shows that the change of AOD effects $f_{\lambda,\theta_v,\theta_s,\varphi}$ is no larger than 0.003 and can be ignored. Another impact on the Earth-to-sensor atmospheric transmission correction factor is the surface BRDF. Since the Sonoran Desert surface BRDF model is difficult to obtain, we refer to the Baotou Desert Site BRDF model to evaluate the influence of surface BRDF on the RTM results. The BRDF model was developed from ground measurements, and the Roujean BRDF model was chosen to calculate the surface reflectance under real geometric conditions. Reference 31 illustrated the construction of the Baotou man-made target BRDF model, and we got the Baotou Desert ground measurements through the Key Laboratory of Quantitative Remote Sensing Information Technology at the Academy of Opto-Electronics Chinese Academy of Science. The sensitivity analysis found that considering the ground BRDF model leads to uncertainty of 0.01 for ABI/NPP and ABI/NOAA-20 comparison. Then TOA radiance and direct-round-reflected radiance can be acquired from MODTRAN simulation outputs. Consequently, the correction factor from RTM simulation for the equivalent channel with central wavelength λ can be calculated as

$$F_{\lambda,\mathrm{VIIRS\_ABI}} = \frac{f_{\lambda,\theta_{\mathrm{VIIRS}},\varphi_{\mathrm{VIIRS}}}}{f_{\lambda,\theta_{\mathrm{ABI}},\varphi_{\mathrm{ABI}}}} = \frac{\dfrac{L_{\lambda,\mathrm{VIIRS}_{\theta_v},\mathrm{VIIRS}_{\theta_s},\mathrm{VIIRS}_{\varphi}}}{l_{\lambda,\mathrm{VIIRS}_{\theta_v},\mathrm{VIIRS}_{\theta_s},\mathrm{VIIRS}_{\varphi}}}}{\dfrac{L_{\lambda,\mathrm{ABI}_{\theta_v},\mathrm{ABI}_{\theta_s},\mathrm{ABi}_{\varphi}}}{l_{\lambda,\mathrm{ABI}_{\theta_v},\mathrm{ABI}_{\theta_s},\mathrm{ABI}_{\varphi}}}}, \tag{9}$$

where $f_{\lambda,\theta_{\mathrm{VIIRS}},\varphi_{\mathrm{VIIRS}}}$ and $f_{\lambda,\theta_{\mathrm{ABI}},\varphi_{\mathrm{ABI}}}$ are the Earth-to-sensor path atmospheric correction factors for VIIRS and ABI at $(\theta_{\mathrm{VIIRS}}, \varphi_{\mathrm{VIIRS}})$ and $(\theta_{\mathrm{GOES}}, \varphi_{\mathrm{GOES}})$, respectively.

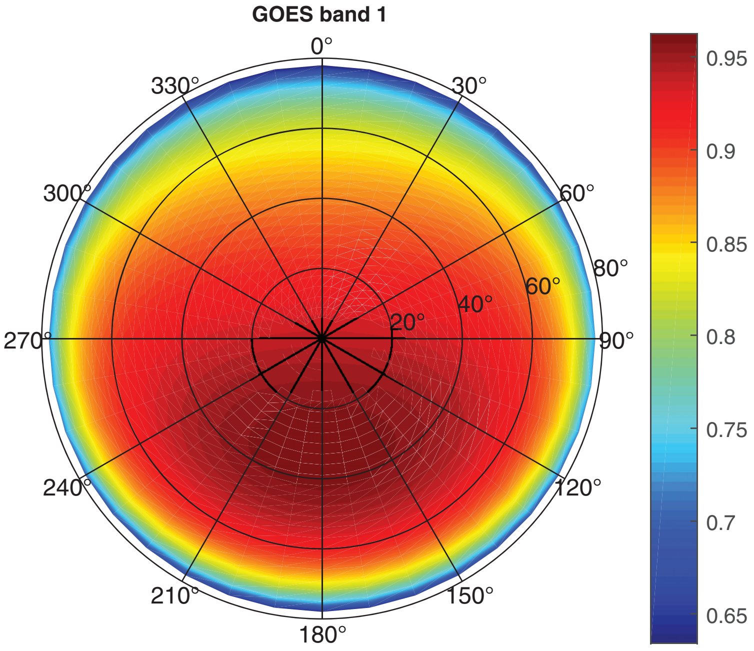

Fig. 9 RTM correction factor between GOES-16 ABI B1 and NPP VIIRS M3 in the coordinate of SZA and RAA with VZA being fixed at 56.35 deg.

To illustrate the impact of SRF factor alone on the ABI VIIRS transmittance difference (RTM-correction factor) along the Earth-to-sensor transmission path through the atmosphere, we set other input factors including RAA, SZA, VZA, and atmosphere profiles to be the same for ABI and VIIRS. Figure 9 shows the distribution of RTM correction factor $F_{470\text{ nm,NPP}-\text{VIIRS,GOES}-\text{ABI}_{\theta_v,\theta_z,\varphi}}$ for GOES-16 ABI B1 and NPP VIIRS M3 as a function of SZA and RAA with VZA being fixed at 56.35 deg, i.e., $\text{VIIRS}_{\theta_v} = \text{GOES}_{\theta_v} = 56.35$ deg, ($\text{VIR}_{\theta_s} = \text{GOES}_{\theta_s}$, $\text{VIIRS}_{\varphi} = \text{GOES}_{\varphi}$). In the polar coordinate, the radius value for each point indicates SZA and the rotation RAA. It can be seen that although under the same VZA and RAA geometry and atmosphere conditions, the variation of $F_{470\text{ nm,NPP}-\text{VIIRS,GOES}-\text{ABI}_{\theta_v,\theta_z,\varphi}}$ has SZA and RAA-dependence, indicating that the SRF difference between two sensors has significant impacts on the Earth-to-sensor atmosphere transmittance.

Therefore, SRF difference between these two sensors cannot be ignored when correcting the impact from Earth-to-sensor atmospheric transmission. Such atmospheric correction factor due to SRF difference of two sensors has not been accounted in the SBAF derived directly from Hyperion observations since the hyperspectral observations are at TOA level.

As discussed above, this work limits RAA between VIIRS and GOES-16 ABI to be within 105 deg to 140 deg and VZA is fixed to be within ±10 deg for VIIRS and GOES-16 ABI. The RTM correction factor with confined VZA and RAA range need to be derived. Figure 10 plots the RTM correction factor $F_{i,\lambda,\text{NPP}-\text{VIIRS,GOES}-\text{ABI}}$ with fixed VZA of 56.35 deg and different combinations of RAAs for GOES and NPP for a specific case i. Note that the color scales for

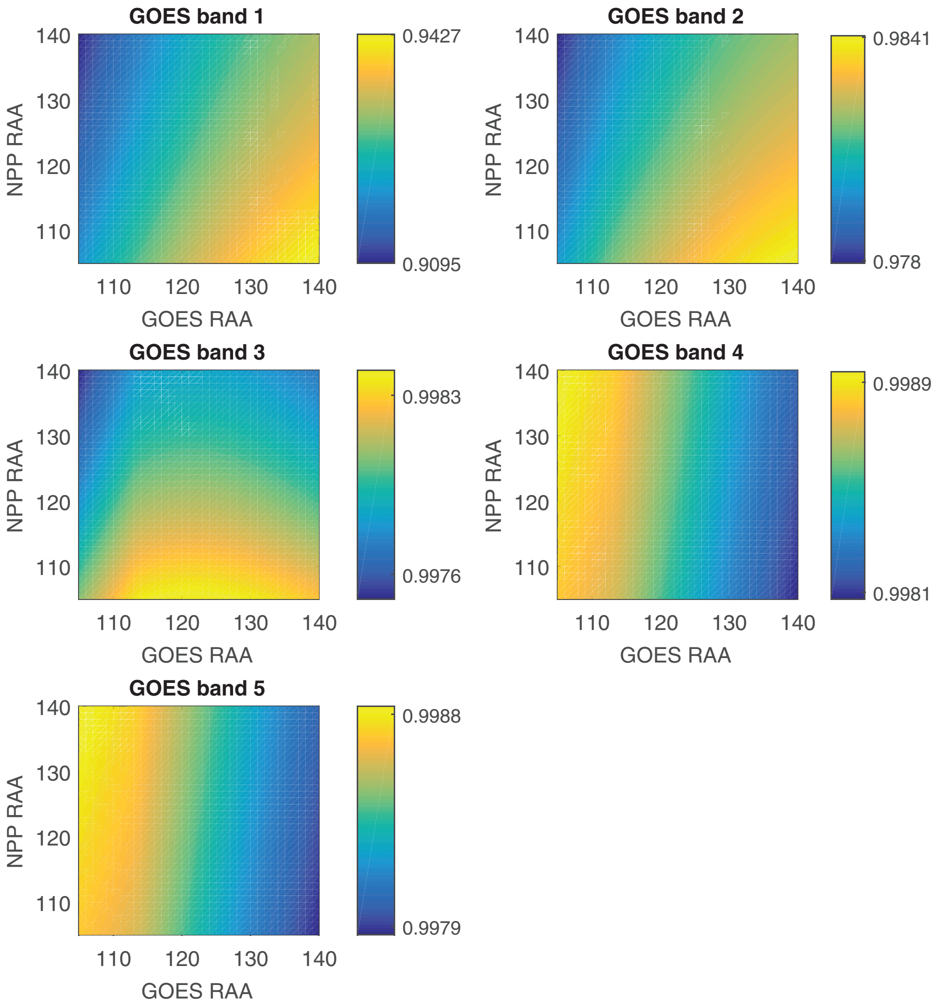

Fig. 10 RTM correction factor $F_{\text{NPP}-\text{VIIRS}-\text{ABI}}$ as a function of the RAA of GOES-16 ABI and NPP VIIRS from 105 deg to 140 deg at the same VZA of 56.35 deg.

the bands are different in this figure to make RAA-dependent variation in the correction factor clearer. It is shown that the RAA-dependent $F_{i,\lambda,\text{NPP-VIIRS,GOES-ABI}}$ of ABI B1 has the largest variability and lowest value compared with other bands. The variation patterns of ABI B1 and B2 are similar with different magnitudes such as varying within [0.91, 0.94] and [0.97, 0.98] for ABI B1 and ABI B2, respectively. The large range of variation in ABI B1 indicates the impacts of Earth-to-sensor atmospheric transmission on two sensors are quite different because of the different SRFs between VIIRS and ABI, which is consistent with the SRF plot in Fig. 2. The values of RAA-dependent $F_{i,\lambda,\text{NPP-VIIRS,GOES-ABI}}$ of ABI B3, B4, and B5 are very close to 1, which suggests that the impacts of atmospheric transmission due to SRF and RAA geometry difference on two sensors are less significant for these three bands. Note that the SBAF in Sec. 3.2 is used for TOA reflectance compensation between ρ_{GOES} and ρ_{VIIRS} because of SRF difference, whereas the RTM correction factor derived in this section accounts for the impact of combined SRF and RAA difference on the Earth-to-Sensor atmospheric transmission.

3.5 *TOA Reflectance Comparison between GOES-16 ABI and SNPP/NOAA-20 VIIRS*

In this study, the TOA reflectance ratio is used as parameter for evaluating consistency among sensors. The reflectance ratios are calculated as

$$R_{i,\lambda,D} = \frac{\rho_{i,\text{GOES}}}{\rho_{i,\text{VIIRS}} \times R_{i,\lambda,\text{VIIRS,GOES\_RAA}} \times \text{SBAF}}, \tag{10}$$

$$R_{i,\lambda,M} = \frac{\rho_{i,\text{GOES}}}{\rho_{i,\text{VIIRS}} \times F_{i,\lambda,\text{VIIRS\_GOES}} \times \text{SBAF}} \tag{11}$$

for DD and RTM-based correction, respectively, for case i, and $\rho_{i,\text{GOES}}$ and $\rho_{i,\text{VIIRS}}$ are the corresponding at-sensor reflectance measurements. The DD correction factor $R_{i,\lambda,\text{VIIRS,GOES\_RAA}}$ is as defined in Eq. (7), RTM correction factor for $F_{i,\text{VIIRS\_GOES}}$ is from Eq. (9), and $R_{i,\lambda,D}$ and $R_{i,\lambda,M}$ are the calibration correction adjustment factors, i.e., reflectance ratios, derived from DD method and RTM method, respectively, for equivalent bands centered at wavelength λ.

4 Results and Discussion

4.1 *GEO-LEO Intercomparison Results and Validation*

4.1.1 *GEO-LEO intercomparison results*

Figure 11(a) shows the time series of reflectance ratio between ABI and VIIRS without correction but with cloud/contamination filtering and VZA/RAA restrictions. The number of data points are significantly reduced in comparison with Fig. 5 because of the angular limitations in RAA and VZA. The annual cycle is largely absent in the time series of reflectance ratio, except for ABI B1. The ABI B1 with central wavelength at 470 nm is sensitive to both the SRF difference between ABI and VIIRS around this band and the atmospheric effect on the transmission of light around this band. In particular, the molecular scattering and aerosol effect on light transmission are largely affected by solar and viewing geometries. The ratio for GOES-16 B2, B3, and B5 are flattened after applying the VZA/RAA restriction since these bands are less sensitive to atmosphere variability and SRF differences. The ratio of GOES-16 B6 is relatively flat but more scattered than other channels, which is consistent with Ref. 7. The possible reason for more scattered B6 ratio is the low-radiance signal, making it very sensitive to changes in the radiation signal. Another notable fact is the drop of reflectance ratio for GOES-16 B2 after April 2019, which can be traced to the modification of ABI calibration coefficients, i.e., the κ parameter (proportional to BRDF) of ABI solar diffuser, for GOES-16 ABI B2 on April 23, 2019. After the GOES-16 ABI calibration coefficient modification, the ABI B2 radiances decreased by about 6.9%[32] and are manifested by consequent drops in ABI versus VIIRS reflectance ratios. In addition, Figure 11(a) also shows that the reflectance ratios between

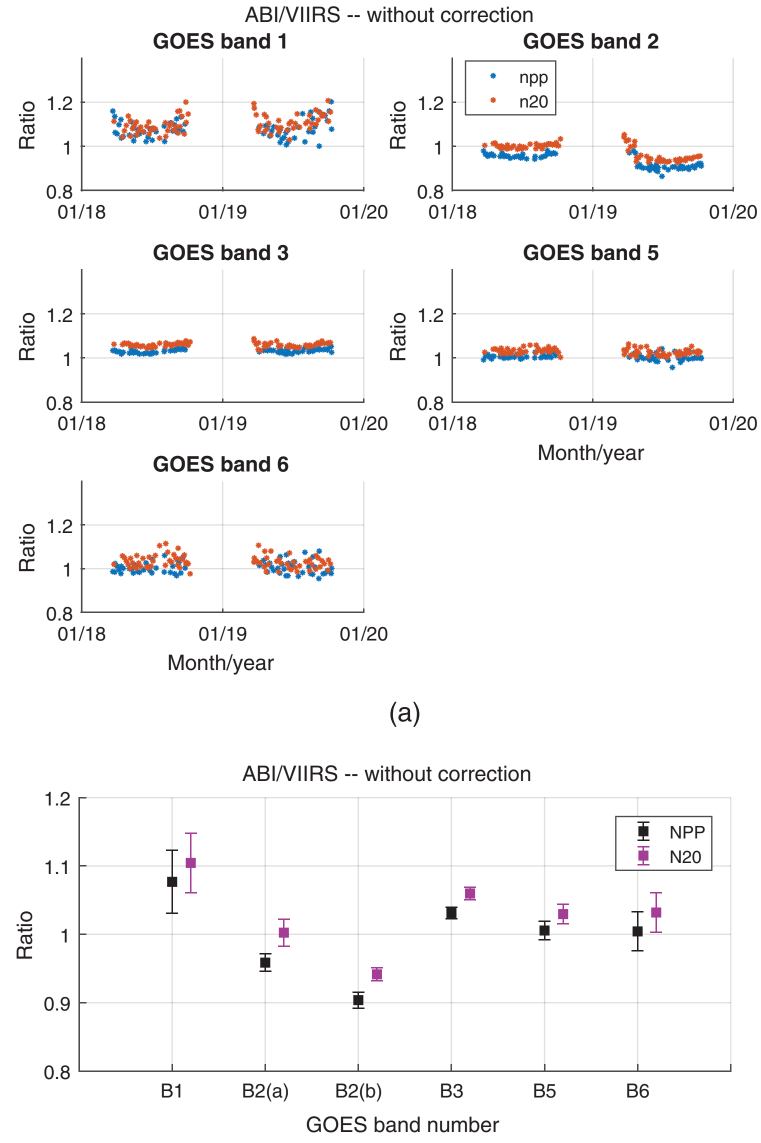

(a)

(b)

Fig. 11 (a) Time series of reflectance ratio of GOES-16 ABI and NPP/NOAA-20 VIIRS. (b) Mean reflectance ratio and its error bar after applying cloud/shadow contamination filtering and VZA/RAA restriction. GOES-16 ABI B2 has been separated into B2(a) and B2(b) corresponding to intervals before and after April 23, 2019.

GOES-16 ABI and NOAA-20 VIIRS are consistently higher than the ratios between GOES-16 ABI and NPP VIIRS for all five VNIR bands.

Figure 11(b) shows the mean reflectance ratio and associated one sigma standard deviation in error bar between GOES-16 ABI and NPP/NOAA-20 VIIRS for the data shown in Fig. 11(a). GOES-16 B2 data have been separated into B2(a) and B2(b) for intervals before and after April 23, 2019, respectively, in Fig. 11(b). Table 3 lists the mean reflectance ratios and their standard deviations for the different bands. GOES-16 ABI B1 has the largest ratio and largest standard deviation, i.e., ~1.10 ± 0.04. GOES-16 ABI B2(b) is ~6% lower in ratio compared to GOES-16 ABI B2(a) due to the ABI calibration coefficients modification.

Figure 12(a) shows the time series of reflectance ratio of ABI and VIIRS using the DD correction method as introduced in Sec. 3.3.1 after the cloud/shadow contamination filtering and SBAF factor have been applied. Compared with Fig. 11(a), the time series of reflectance ratios between GOES ABI and NPP/NOAA-20 VIIRS for five band show mixed results.

Table 3 Mean and standard deviation of GEO-LEO reflectance ratio without correction, using DD and RTM-based methods, respectively. GOES-16 ABI B2 has been separated into B2(a) and B2(b) corresponding to intervals before and after April 23, 2019.

	GOES-16 ABI/NPP VIIRS			GOES-16 ABI/NOAA-20 VIIRS		
	Without correction	DD method	RTM method	Without correction	DD method	RTM method
B1	1.08 ± 0.05	1.12 ± 0.03	1.05 ± 0.03	1.10 ± 0.04	1.16 ± 0.03	1.08 ± 0.03
B2(a)	0.96 ± 0.01	1.03 ± 0.02	1.01 ± 0.02	1.00 ± 0.02	1.05 ± 0.02	1.04 ± 0.03
B2(b)	0.90 ± 0.01	0.97 ± 0.02	0.96 ± 0.02	0.94 ± 0.01	0.99 ± 0.02	0.98 ± 0.02
B3	1.03 ± 0.01	1.02 ± 0.01	1.03 ± 0.01	1.06 ± 0.01	1.05 ± 0.01	1.06 ± 0.01
B5	1.01 ± 0.01	0.99 ± 0.02	1.00 ± 0.01	1.03 ± 0.01	1.02 ± 0.02	1.03 ± 0.02
B6	1.00 ± 0.03	0.96 ± 0.03	0.97 ± 0.03	1.03 ± 0.03	0.98 ± 0.03	1.00 ± 0.03

The reflectance ratio of ABI B1 is relatively flatter, that is, the annual cycle variation caused by viewing geometry variation has been largely corrected. However, there is some residual reversed annual variation in ABI B1 reflectance ratio data. As noted in Secs. 3.3.1 and 3.3.2, the unaccounted angular dependence of impact of atmospheric scattering on GOES-16 ABI B1 is the most likely reason for such large increase of reflectance ratio and need to be corrected with RTM-based correction factor. The temporal variation of reflectance ratios for ABI band 2, 3, and 5 are similar to those in Fig. 11(a). In addition, the fact that GOES-16 ABI versus NPP VIIRS ratios are higher than the ratio between GOES-16 ABI and NOAA-20 VIIRS and the drop of ratio for ABI B2 after April 2019 remain clear in Fig. 12(a).

Figure 12(b) shows the mean reflectance ratio between GOES-16 ABI and NPP/NOAA-20 VIIRS after applying the DD correction together with the associated error bar. Table 3 lists the corresponding mean reflectance ratio and standard deviation values with DD correction. The values of the reflectance ratio for GOES-16 ABI B1 with respect to SNPP and NOAA-20 VIIRS are 1.12 and 1.16, respectively, which are unreasonably higher than those (∼1.06) expected from other studies.[12,32]

Figure 13 shows the time series of reflectance ratio of GOES-16 ABI versus NPP/NOAA-20 VIIRS for five bands using Eq. (11), i.e., the RTM method as prescribed in Sec. 3.3.2. The cloud/shadow contamination filtering and SBAF factor have been applied. Since the atmosphere correction factors along Earth-to-sensor transmission path, i.e., $F_{\lambda,\text{VIIRS\_ABI}}$, are all close to 1 for ABI B3, B5, and B6 as seen from Fig. 10 with correction factors ranging from 0.9976 to 0.9988, the reflectance ratios are quite similar to those show in Fig. 11 before applying the RTM-correction factor. On the other hand, the most significant change occurs for ABI B1 where the annual cycle variation in the time series of reflectance ratio is efficiently removed with the RTM-correction method. Moreover, the mean reflectance ratio value of ABI B1 becomes reasonable after using the RTM correction in comparison with the mean reflectance ratio value using DD correction. For ABI B6, given the low solar irradiance and higher noise, the reflectance ratio remains as scattered during summer season as those shown in Fig. 11.

Figure 13(b) shows the mean reflectance ratios between GOES-16 ABI and NPP/NOAA-20 VIIRS after applying the RTM method correction and error bars. Table 3 lists the corresponding mean ratio values and associated standard deviations. The reflectance ratio between GOES-16 ABI and NPP VIIRS for ABI B1 is ∼1.05, which is consistent with the result from previous results[12,33] obtained using other independent methods. The reflectance ratio of GOES-16 ABI B2(b) with respect to SNPP VIIRS is ∼0.97, after the ABI calibration coefficient modification for ABI B2 after April 23, 2019. In a previous evaluation[12] using co-location method, the reflectance ratio between ABI B6 and NPP VIIRS M11 is ∼1.03, whereas the ratio derived in this paper is 0.97. Part of the difference is due to that the SBAF correction between ABI B6 and VIIRS M11 was not applied in Ref. 12.

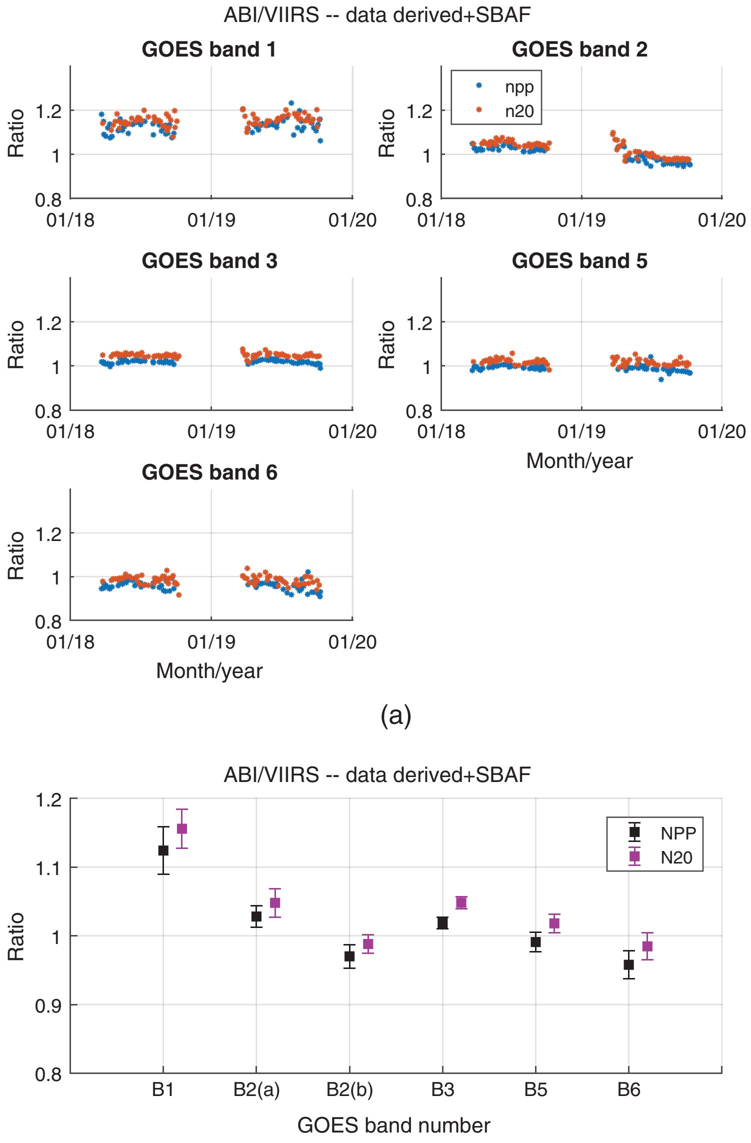

(a)

(b)

Fig. 12 (a) Time series of reflectance ratio between GOES-16 ABI and NPP/NOAA-20 VIIRS for five bands. (b) Mean reflectance ratio and associated error bar after applying DD correction method. The cloud/shadow contamination filtering and SBAF factor has also been applied. Evaluation of GOES-16 ABI B2 reflectance ratio has been separated into B2(a) and B2(b) corresponding to intervals before and after April 23, 2019.

4.1.2 *GEO-LEO intercomparison results validation*

To validate the GEO-LEO intercomparison results and evaluate the two geometry correction methods, the previous study results are referred in this section. Uprety et al.[12,13] showed that the reflectance ratio biases between ABI and VIIRS are within 0.05 over Libya 4 desert site from May 2018 to May 2019. Yu et al.[2] reported that the initial solar calibration accuracy of ABI is within 5% difference from VIIRS for B01, B03, B05, and B06. The mean reflectance ABI B2 is 8.1% brighter than VIIRS I2 (0.64 μm). It was reported that ABI B2 initial solar calibration coefficients were also about 7% to 8% larger than the prelaunch value.[2] Bhatt et al.[34] used all-sky tropical ocean ray matching (ATO-RM) and deep convective cloud invariant target (DCC-IT) methods and reported that the ABI and VIIRS RSB calibration are within 5%, except for the 0.47-μm band, for which the radiometric inconsistency is found to be ~7%. McCorkel et al.,[7] using a 5-day field campaign, showed that the accuracy of the ABI reflective

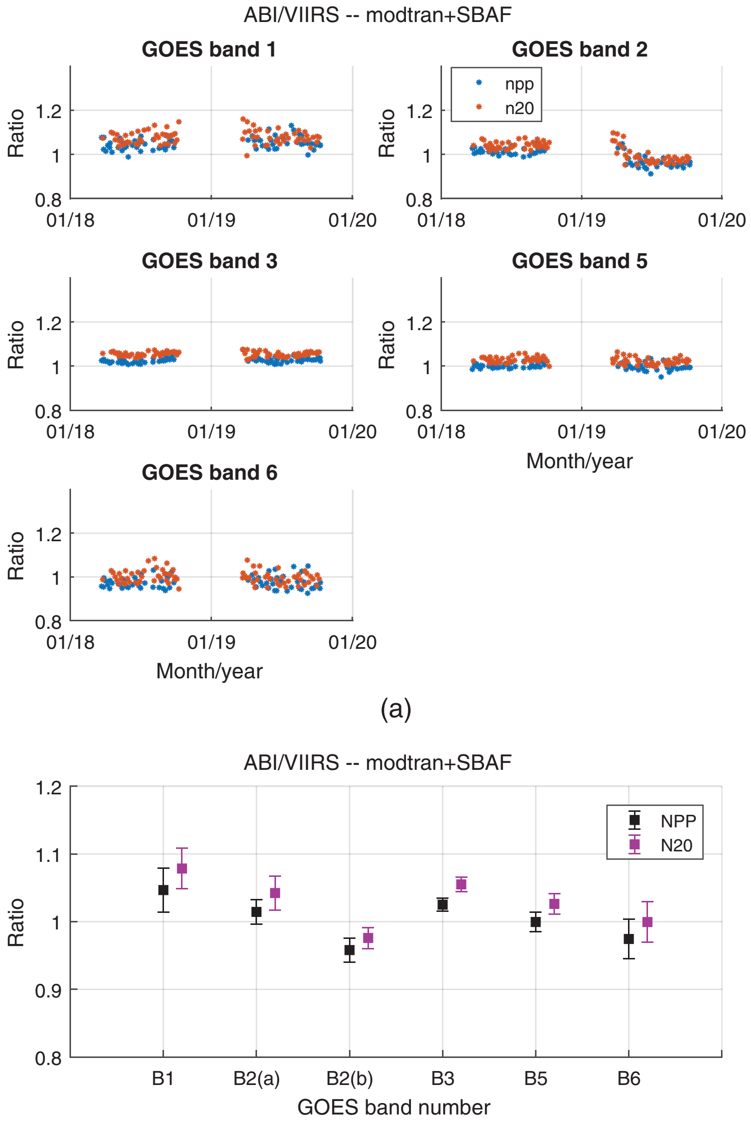

(a)

(b)

Fig. 13 (a) Time series of reflectance ratio between GOES-16 ABI and NPP/NOAA-20 VIIRS for five bands. (b) Mean reflectance ratio and associated error bar after applying RTM correction method. The cloud/shadow contamination filtering and SBAF factor have been applied.

channels calibration is within specification for channels 1, 3, 5, and 6—average biases within 2%; for channel 2 the bias is 5%.

The results of these previous studies and our results are summarized in Table 4. Yu et al.[2] and the vicarious calibration work[7] did not provide the result for ABI B2 after April 23, 2019. And we did not include the results for ABI B2 and B5 from Ref. 34 because the reference channels for these two are VIIRS I1 and I3, respectively, which are not very referential. Figure 14 shows the mean and standard deviation of the results of the radiometric comparison of GEOS ABI and NPP VIIRS measurements obtained from previous studies and from our study. "Mean" in the legend indicates the weighted mean ratio and propagated standard deviation of the results from previous studies.

It can be seen that the adjustment by DD and RTM methods are channel-dependent. For B3, B5 channels, DD and RTM-corrected and the results without correction are quite consistent (difference <1%). Because the SBAF of these two channels close to 1, and DD and RTM correction factors are close to 1 too, indicating for the channels less affected by SRF and geometry difference, DD and RTM methods will not over or under correct them. For B6, DD and RTM

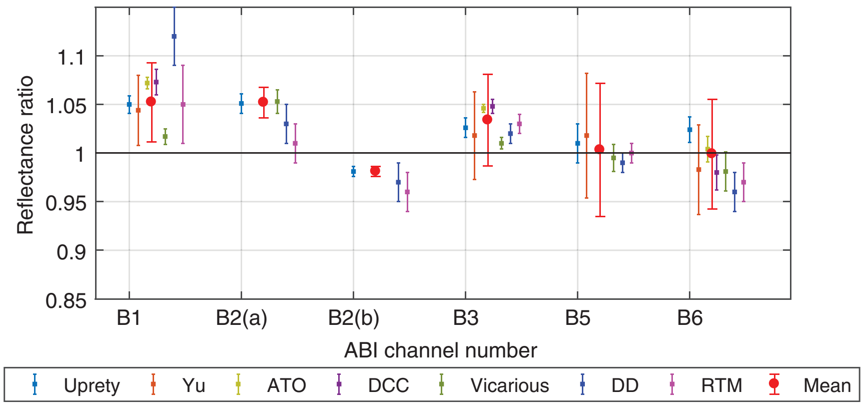

Fig. 14 The mean and standard deviation of the results of the radiometric comparison of GEOS ABI and NPP VIIRS measurements obtained from previous studies and from our study. Mean indicates the weighted mean ratio and propagated standard deviation of the results from the previous studies.

corrected original results by 0.04 and 0.03, respectively, compared with previous result. This is correction mainly due to the SBAF correction factor of B6, which is 1.03. Considering the large standard deviation of B6 previous mean and most previous results are around 0.98, the corrected results are acceptable. For B1, this channel is affected by atmosphere scattering the most and the DD method inversely adjusted the original result and reaches to 1.12, which is too far from the previous results. On the other hand, B1 RTM factors (range from 0.9 to 0.943) and B1 SBAF (0.954) are combined to correct the original result to a reasonable value, which is 1.05, indicating the RTM factor effectively eliminates the residual atmosphere error that DD method cannot remove. For B2 channel, both DD and RTM corrected original results to some extent. However, the lower biases for ABI B2(a) determined from RTM method in comparison with other independent studies needs further investigation.

Generally, the radiometric biases of five VNIR channels of GOES ABI all agree well with S-NPP VIIRS to be within 5% after applying the DD or RTM correction except the remaining ~11% bias in the DD correction of ABI B1. Considering the standard deviation from this analysis, the results derived with DD and RTM methods are statistically consistent with the mean biases derived in previous studies.[2,7,12,13,34] for all of the five ABI bands except for B1 with DD method and B2(a) with RTM method. In general, RTM method results are more consistent with previous results (Table 4 mean ratios) than DD results except for ABI B2 band. Therefore, the RTM method most effectively corrects the residual biases for ABI B1 that is affected by atmospheric scattering the most.

4.2 *Evaluation of Radiometric Bias Between NPP and NOAA-20 VIIRS Using Double Difference Method*

In the previous section, both NPP VIIRS and NOAA-20 VIIRS VNIR channel measurements over the Sonoran Desert were used as the reference sensor for evaluating the radiometric performance of five bands of GOES-16 ABI. Alternatively, the LEO-GEO reflectance ratio derived in Sec. 4.1 can be used to evaluate the relative bias between NPP and NOAA-20 VIIRS using double difference method. This method uses the relative radiometric response ratio D between NPP and NOAA-20 VIIRS after applying the double difference method on the LEO-GEO reflectance ratio:

$$D = \frac{R_{\mathrm{GOES\_N20}}}{R_{\mathrm{GOES\_NPP}}}, \tag{12}$$

where $R_{\mathrm{GOES\_N20}}$ and $R_{\mathrm{GOES\_NPP}}$ are the are the LEO-GEO reflectance ratios derived in Sec. 3.4 for GOES-16 ABI versus NOAA-20 VIIRS and GOES-16 ABI versus NPP VIIRS, respectively.

Table 4 The summary of the results of the radiometric comparison of GEOS ABI and NPP VIIRS measurements obtained from previous studies and from our study

	GOES-16 ABI/NPP VIIRS							
	Uprety	Yu	ATO-RM	DCC-IT	Vicarious	Mean of previous	DD	RTM
B1	1.050 ± 0.009	1.044 ± 0.036	1.072 ± 0.006	1.073 ± 0.013	1.017 ± 0.008	1.052 ± 0.041	1.12 ± 0.03	1.05 ± 0.03
B2(a)	1.051 ± 0.010	1.081 ± 0.051	N/A	N/A	1.053 ± 0.012	1.052 ± 0.016	1.03 ± 0.02	1.01 ± 0.02
B2(b)	0.981 ± 0.005	N/A	N/A	N/A	N/A	0.981 ± 0.005	0.97 ± 0.02	0.96 ± 0.02
B3	1.026 ± 0.010	1.018 ± 0.045	1.046 ± 0.004	1.048 ± 0.007	1.010 ± 0.006	1.034 ± 0.047	1.02 ± 0.01	1.03 ± 0.01
B5	1.010 ± 0.020	1.018 ± 0.064	N/A	N/A	0.995 ± 0.014	1.003 ± 0.069	1.00 ± 0.02	1.00 ± 0.01
B6	1.024 ± 0.013	0.983 ± 0.046	1.004 ± 0.013	0.980 ± 0.018	0.981 ± 0.020	0.999 ± 0.056	0.96 ± 0.03	0.97 ± 0.03

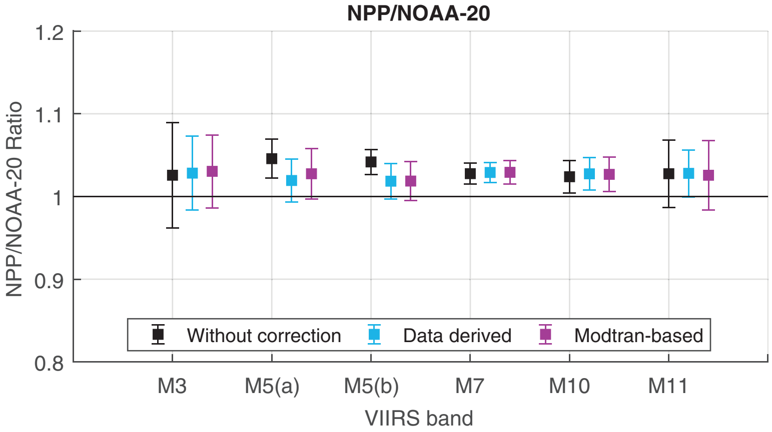

Fig. 15 Relative reflectance ratio between NPP and NOAA-20 VIIRS for five bands together with the error bars derived ROM double-difference using GOES-16 ABI and the transfer reference sensor for evaluations without correction (Fig. 11), using DD (Fig. 12) and using RTM (Fig. 13) corrections.

The LEO-GEO reflectance ratios used in double difference method can be without correction (Fig. 11), with DD (Fig. 12) correction or with RTM correction (Fig. 13).

The LEO-LEO, i.e., NPP versus NOAA-20, reflectance ratio results for five VIIRS bands corresponding to without SBAF and viewing geometry correction and, with DD-correction and RTM-correction are plotted in Fig. 15. Table 5 lists the corresponding mean NPP versus NOAA-20 reflectance ratios and their combined standard deviations. The mean LEO-LEO ratios with DD and RTM corrections are similar to the ratios before applying the correction for VIIRS M7, M10, and M11 channels. The largest change in LEO-LEO reflectance ratio after applying two correction methods in comparison with the ratio without correction is for VIIRS M5 (equivalent to GOES-16 B2). This is because VIIRS M5 has the largest SBAF factor difference between NPP and NOAA-20, i.e., 0.9268 versus 0.9472, as shown in Table 2. Similar conditions hold for VIIRS M3 (equivalent to GOES-16 B1), as the LEO-LEO reflectance ratio changes slightly after the two correction methods are applied to account for the SBAF difference between NPP and NOAA-20 for this band. The LEO-LEO mean reflectance ratios derived with DD and RTM correction methods for all bands are quite consistent. After the two correction methods have been applied, the NPP versus NOAA-20 reflectance ratios are consistently around 1.03. This result is consistent with a previous evaluation using co-location method to derive LEO-GEO bias then LEO-LEO bias using double difference method.[35] Since both LEO sensors observe

Table 5 Mean and standard deviation of NPP versus NOAA-20 reflectance ratios for evaluations of relative radiometric bias using without SBAF and viewing geometry, DD, and RTM correction methods, respectively.

	NPP/NOAA-20		
	Without correction	DD method	RTM method
M3	1.03 ± 0.06	1.03 ± 0.04	1.03 ± 0.04
M5(a)	1.05 ± 0.02	1.03 ± 0.03	1.03 ± 0.03
M5(b)	1.04 ± 0.02	1.02 ± 0.03	1.02 ± 0.02
M7	1.03 ± 0.01	1.03 ± 0.02	1.03 ± 0.01
M10	1.02 ± 0.02	1.03 ± 0.03	1.03 ± 0.02
M11	1.03 ± 0.04	1.03 ± 0.05	1.03 ± 0.04

the same desert site and after applying either the DD or RTM correction method, LEO-LEO reflectance ratios are consistent, our results suggest that NOAA-20 VIIRS are radiometrically biased lower than S-NPP VIIRS by about 2% to 3% for all of the five VNIR bands of interest.

5 Conclusion

The radiometric performance of GOES-16 ABI VNIR bands (B1, B2, B3, B5, and B6) is evaluated in this paper, with the Sonoran Desert (32.05° N–32.35° N, 114.7° W–114.4° W), which is one of the largest deserts in North America, used as the PICS. The evaluation is based on intercomparison of GOES-16 ABI VNIR bands (B1, B2, B3, B5, and B6) with NPP and NOAA-20 VIIRS measurements at matched VNIR bands (M3, M5, M7, M10, and M11). In addition, the NPP versus NOAA-20 VIIRS radiometric consistency over these five VNIR bands are also evaluated through double difference of GEO-LEO comparison results. To remove the effects of residual viewing geometry difference between GOES-16 ABI and NPP/NOAA-20 VIIRS, two correction methods, namely, DD and RTM, have been developed and applied separately to make corrections to the directly derived LEO-GEO radiometric bias. This evaluation of the radiometric performance of GOES-16 ABI relative to NPP and NOAA-20 VIIRS using these two correction methods addresses the deficiencies in the DD correction method by showing the improvements made with the RTM-based correction.

After preprocessing the LEO and GEO data, either DD or RTM correction method is combined with SBAF correction to evaluate the LEO-GEO radiometric bias. The SBAF correction factors derived from Hyperion observations show that GOES-16 ABI (B1 and B2) have the largest correction values. The DD or RTM correction method is used in this paper to remove the impacts of residual RAA geometry difference between GOES-16 ABI and NPP/NOAA-20 VIIRS. It is found that the DD method could not correct the unaccounted bias between ABI B1 and VIIRS M3 due to the effect of atmospheric scattering on the radiation transmission path difference between ABI and VIIRS for these channels. Therefore, the RTM correction method, which accounts for the differences in atmospheric transmission path, spectral and view geometry between ABI and VIIRS, is developed to address the deficiency in the DD correction method.

For all the ABI channels, the magnitudes of radiometric bias correction are similar between applying DD and RTM correction except for ABI B1 for which the radiometric bias correction from two methods differs by 7% to 8%. The large difference for ABI B1 is mainly caused by the unaccounted atmospheric scattering along the Earth-to-sensor atmospheric transmission-path due to different ABI and VIIRS view geometries. After applying the RTM-based correction, the mean reflectance ratio values are 1.05 and 1.08 for ABI B1 relative to NPP and NOAA-20 VIIRS, respectively, which are consistent with results from previous independent evaluations.

In summary, the radiometric biases of all five GOES ABI VNIR channels were within 5% agreement with the S-NPP VIIRS after using the RTM corrections. In addition, our analysis also detected the ∼6% radiometric bias drop for ABI B2 after April 23 2019 due to the calibration update for GOES-16 ABI. These results are consistent with the results from previous studies using other independent methods, except that differences with ABI B2(a) need to be explored further.

This paper also evaluates the radiometric biases between NPP and NOAA-20 VIIRS for the five matching ABI VNIR channels through double difference. Before the DD or RTM correction method is applied, the radiometric bias of VIIRS M5 between NPP and NOAA-20 is unphysically large (∼5%) due to the relatively large difference in their SRFs, which can be seen from the SBAF factor difference between NOAA-20 and NPP (Table 2) for this channel. After DD or RTM correction, our results suggest that NOAA-20 VIIRS bands TOA reflectance are lower than S-NPP VIIRS by about 2% to 3%. This result is consistent with the NPP versus NOAA-20 VIIRS bias evaluation from previous analysis using the co-location method to derive the LEO-GEO bias and then evaluate the LEO-LEO bias using the double difference method.[32]

The PICS-based GEO-LEO and LEO-LEO intercomparison method developed in this paper can be applied to measurements over other calibration sites such as desert and snow flats and supports evaluation of intersensor bias between other geostationary satellite sensors such as HIMAWARI Advanced Himawari Imager (AHI) series, GOES-17 ABI, and LEO sensors such as MODIS, VIIRS, and the future METimage on METOP-SG mission.

Acknowledgments

This study was supported by National Oceanic and Atmospheric Administration Grant (No. NA19NES4320002) (Cooperative Institute for Satellite Earth System Studies—CISESS) at the University of Maryland/ESSIC. We thank the helpful discussions with Jun Dong and his assistance in collecting data.

References

1. T. J. Schmit et al., “A closer look at the ABI on the GOES-R series,” *Bull. Am. Meteorol. Soc.* **98**(4), 681–698 (2017).
2. F. Yu et al., “Early radiometric calibration performances of GOES-16 advanced baseline imager,” *Proc. SPIE* **10402**, 104020S (2017).
3. F. Yu et al., “Validation of early GOES-16 ABI on-orbit geometrical calibration accuracy using SNO method,” *Proc. SPIE* **10402**, 104020U (2017).
4. S. Kalluri et al., “From photons to pixels: processing data from the advanced baseline imager,” *Remote Sens.* **10**(2), 177 (2018).
5. J. P. Fulbright et al., “Calibration/validation strategy for GOES-R L1b data products,” *Proc. SPIE* **10000**, 100000T (2016).
6. R. Bhatt et al., “Advances in utilizing tropical deep convective clouds as a stable target for on-orbit calibration of satellite imager reflective solar bands,” *Proc. SPIE* **11127**, 111271H (2019).
7. J. McCorkel et al., “GOES-16 ABI solar reflective channel validation for earth science application,” *Remote Sens. Environ.* **237**, 111438 (2020).
8. G. Chander et al., “Overview of intercalibration of satellite instruments,” *IEEE Trans. Geosci. Remote Sens.* **51**(3), 1056–1080 (2013).
9. F. Yu et al., “Intercalibration of GOES Imager visible channels over the Sonoran Desert,” *J. Geophys. Res. Atmos.* **119**(14), 8639–8658 (2014).
10. J. S. Czapla-Myers and N. J. Anderson, “Post-launch radiometric validation of the GOES-16 advanced baseline imager (ABI),” *Proc. SPIE* **10785**, 107851F (2018).
11. H. Yoo, F. Yu, and X. Wu, “Site selection and characterization at Uyuni desert for the calibration and validation of GOES-16 ABI solar reflective bands,” *Proc. SPIE* **10402**, 104022M (2017).
12. S. Uprety, C. Cao, and X. Shao, “Geo-Leo intercalibration to evaluate the radiometric performance of NOAA-20 VIIRS and GOES-16 ABI,” *Proc. SPIE* **11127**, 111270S (2019).
13. S. Uprety and C. Cao, “Radiometric and spectral characterization and comparison of the Antarctic Dome C and Sonoran Desert sites for the calibration and validation of visible and near-infrared radiometers,” *J. Appl. Remote Sens.* **6**(1), 063541 (2012).
14. D. L. Morstad and D. L. Helder, “Use of pseudo-invariant sites for long-term sensor calibration,” in *IEEE Int. Geosci. and Remote Sens. Symp.*, IEEE, Vol. 1, p. I-253 (2008).
15. A. Angal et al., “Characterization of the Sonoran Desert as a radiometric calibration target for Earth observing sensors,” *J. Appl. Remote Sens.* **5**(1), 059502 (2011).
16. “GOES-R product definition and users’ guide (PUG),” Vol. 3, Level 1b Products, Harris Corporation, https://www.goes-r.gov/users/docs/PUG-L1b-vol3.pdf (2019).
17. S. Uprety and C. Cao, “Suomi NPP VIIRS reflective solar band on-orbit radiometric stability and accuracy assessment using desert and Antarctica Dome C sites,” *Remote Sens. Environ.* **166**, 106–115 (2015).
18. S. Uprety et al., “Radiometric intercomparison between Suomi-NPP VIIRS and Aqua MODIS reflective solar bands using simultaneous nadir overpass in the low latitudes,” *J. Atmos. Ocean. Technol.* **30**(12), 2720–2736 (2013).
19. C. Cao et al., “Suomi NPP VIIRS sensor data record verification, validation, and long-term performance monitoring,” *J. Geophys. Res. Atmos.* **118**(20), 11,664–11,678 (2013).
20. P. Barry, “EO-1 hyperion science data user’s guide,” TRW Space, Defense & Information Systems. One Space Park Redondo Beach, CA, 2001, https://eo1.gsfc.nasa.gov/new/general/Disk2/HyperionScienceDataUsersGuide_public_L1B.pdf (accessed on 5 March 2019).

21. E. M. Middleton et al., "The Earth Observing One (EO-1) satellite mission: over a decade in space," *IEEE J. Sel. Top. Appl. Earth Obs. Remote Sens.* **6**(2), 243–256 (2013).
22. J. Czapla-Myers et al., "Validation of EO-1 hyperion and advanced land imager using the radiometric calibration test site at Railroad Valley, Nevada," *IEEE J. Sel. Top. Appl. Earth Obs. Remote Sens.* **9**(2), 816–826 (2016).
23. X. Jing et al., "Lifetime absolute calibration of the EO-1 Hyperion sensor and its validation," *IEEE Trans. Geosci. Remote Sens.* **57**(11), 9466–9475 (2019).
24. F. Yu and X. Wu, "Removal of contaminated pixels from the desert target for AVHRR vicarious calibration," *J. Atmos. Ocean. Technol.* **26**(7), 1354–1366 (2009).
25. D. L. Smith and C. V. Cox, "(A) ATSR solar channel on-orbit radiometric calibration," *IEEE Trans. Geosci. Remote Sens.* **51**(3), 1370–1382 (2013).
26. X. Wu, J. T. Sullivan, and A. K. Heidinger, "Operational calibration of the advanced very high resolution radiometer (AVHRR) visible and near-infrared channels," *Can. J. Remote Sens.* **36**(5), 602–616 (2010).
27. G. Chander et al., "Applications of spectral band adjustment factors (SBAF) for cross-calibration," *IEEE Trans. Geosci. Remote Sens.* **51**(3), 1267–1281 (2013).
28. P. M. Teillet et al., "Impacts of spectral band difference effects on radiometric cross-calibration between satellite sensors in the solar-reflective spectral domain," *Remote Sens. Environ.* **110**(3), 393–409 (2007).
29. A. Angal et al., "Using the Sonoran and Libyan Desert test sites to monitor the temporal stability of reflective solar bands for Landsat 7 enhanced thematic mapper plus and Terra moderate resolution imaging spectroradiometer sensors," *J. Appl. Remote Sens.* **4**(1), 043525 (2010).
30. Inness et al., "CAMS global reanalysis (EAC4)," 2019, https://ads.atmosphere.copernicus.eu/cdsapp#!/dataset/cams-global-reanalysis-eac4?tab=form (accessed 28 November 2020).
31. M. Zhihong et al., "A method for hyperspectral reflectance reconstruction from automatic observation with multispectral radiometer," *Acta Opt. Sin.* **39**(7), 0728004 (2019).
32. S. Lindstrom et al., "GOES-R band 2 ('red visible') calibration changes," 2019, https://cimss.ssec.wisc.edu/satellite-blog/archives/33083 (accessed 28 November 2020).
33. X. Shao et al., "Validation of GOES-16 ABI reflective solar band calibration through reanalysis and comparison with field campaign data," *Proc. SPIE* **10764**, 107640I (2018).
34. R. Bhatt et al., "Clouds and the Earth's radiant energy system strategy for intercalibrating the new-generation geostationary visible imagers," *J. Appl. Remote Sens.* **14**(3), 032410 (2020).
35. S. Uprety et al., "Evaluating NOAA-20 and S-NPP VIIRS radiometric consistency," *Proc. SPIE* **10781**, 107810V (2018).

Xin Jing received her BS degree in mapping and surveying from Tongji University, Shanghai, China, in 2007, and her MS and PhD degrees in remote sensing from Peking University, Beijing, China, in 2012 and 2017, respectively. She is a postdoctoral associate at the University of Maryland. Her current research interests include vicarious calibration, temporal trending, and validation of GEO/LEO sensors.

Tung-Chang Liu received his BS degree in physics from the National Taiwan University, Taipei, Taiwan, and PhD in physics from the University of Maryland, College Park, Maryland, USA, in 2013. His research interest includes laser plasma interaction and laser proton accelerator design and applications, remote sensing imagery data analysis and correction, and modeling of calibration system for imaging sensor.

Biographies of the other authors are not available.